Hindawi Publishing Corporation
International Journal of Antennas and Propagation
Volume 2015, Article ID 129823, 18 pages
http://dx.doi.org/10.1155/2015/129823

Research Article

A Simple Quantitative Inversion Approach for Microwave Imaging in Embedded Systems

M. Ambrosanio,[1] R. Scapaticci,[2] and L. Crocco[2]

[1] *University of Naples "Parthenope", 80143 Naples, Italy*
[2] *IREA, National Research Council of Italy, 80124 Naples, Italy*

Correspondence should be addressed to R. Scapaticci; scapaticci.r@irea.cnr.it

Received 20 February 2015; Accepted 31 May 2015

Academic Editor: Felipe Cátedra

Copyright © 2015 M. Ambrosanio et al. This is an open access article distributed under the Creative Commons Attribution License, which permits unrestricted use, distribution, and reproduction in any medium, provided the original work is properly cited.

In many applications of microwave imaging, there is the need of confining the device in order to shield it from environmental noise as well as to host the targets and the medium used for impedance matching purposes. For instance, in MWI for biomedical diagnostics a coupling medium is typically adopted to improve the penetration of the probing wave into the tissues. From the point of view of quantitative imaging procedures, that is aimed at retrieving the values of the complex permittivity in the domain under test, the presence of a confining structure entails an increase of complexity of the underlying modelling. This entails a further difficulty in achieving real-time imaging results, which are obviously of interest in practice. To address this challenge, we propose the application of a recently proposed inversion method that, making use of a suitable preprocessing of the data and a scenario-oriented field approximation, allows obtaining quantitative imaging results by means of quasi-real-time linear inversion, in a range of cases which is much broader than usual linearized approximations. The assessment of the method is carried out in the scalar 2D configuration and taking into account enclosures of different shapes and, to show the method's flexibility different shapes, embedding nonweak targets.

1. Introduction

Microwave imaging (MWI) is an emerging and appealing technique to retrieve morphological and quantitative maps of the electromagnetic properties of notaccessible domains. The physical phenomenon which MWI is based on is the electromagnetic scattering, which is due to differences in the electromagnetic properties of the targets with respect to those of the background. Based on this principle, there is a number of applications in which MWI is finding place, ranging from civil engineering to cultural heritage and archaeology, from security to medical diagnostics [1].

Owing to such a remarkably broad range of applications, several efforts have been carried out and are ongoing in the design of accurate imaging devices and in the development of reliable strategies for the processing of the data. In particular, these latter represent a challenging task, as they have to cope with the nonlinearity and ill-posedness of the inverse problem underlying MWI.

Among the various applications, one that has gained a growing interest is that of biomedical diagnostics, wherein the interest in MWI is mainly motivated by the nonionizing nature of microwave radiations and their potential of providing quantitative images through relatively low cost devices.

In such a framework, microwave imaging systems are typically confined, that is, delimited by a metallic or dielectric casing. The role of such a casing is twofold. On the one hand, it is meant to isolate the apparatus from external interference. On the other, it has to contain the coupling medium (usually liquid) in which the target of the diagnostic survey is embedded and which is adopted to facilitate the penetration of the probing wave inside the inspected tissues and maximize their interaction. Some examples of such systems are the system for breast cancer imaging developed at Dartmouth College [2], the scanner developed at the Institute Fresnel [3], and the imaging system of Manitoba University [4].

On the other hand, the presence of a confining structure implies a considerable increase in the complexity of the interaction between the field and the target. This entails that, in the development of any inversion strategy of the data, an adequate electromagnetic modeling of the actual system is necessary.

While canonical cases (such as a cylindrical circular cross section embedding) can be accounted for by means of analytic tools [5, 6], in more complex scenarios the use of appropriate numerical techniques is the obvious solution. For instance, several authors have pursed the hybridization of iterative inversion techniques based on gradient optimization with forward solver and modeling based on the Finite Element Method (FEM) [7]. This is, for instance, the case of the works by Lencrerot and coworkers [8], that have exploited a FEM solver as the forward engine of a Netwton Kantorovich approach, by Zakaria and coworkers [9], that have proposed a hybrid FEM contrast source inversion scheme, and by Attardo et al. who have introduced a FEM based contrast source extended Born inversion scheme [10].

While the abovementioned approaches are certainly effective ways to tackle the inverse scattering problem in a noncanonical configuration, such as the one in which the system is enclosed into a shielding, they have a drawback related to their nonnegligible computational cost deriving from their iterative nature. This circumstance prevents them from providing real-time or quasi-real-time imaging results. In addition, as they tackle the nonlinear problem through a local optimization scheme, they are prone to the occurrence of false solutions, which is an obviously detrimental outcome in any imaging application, but it is even worse in medical applications.

On the downside, approaches based on the linearization arising from the Born approximation (BA) [1, 11, 12], as well as shape reconstruction methods [13–15], could met the computational efficiency required to provide real-time results, but they are not able to provide quantitative images, which represent the true added value of MWI. Moreover, methods based on the BA have a limited range of applicability, as they can be indeed confidently applied only for weakly scattering targets [16].

With respect to such a scenario, this paper presents the application of a recently proposed inversion method [17] to the case of embedded imaging systems. The considered method has the unique capability of handling the quantitative imaging of nonweak targets within a linear framework. This is accomplished by exploiting an original field approximation that stems from an original exploitation of the well-known Linear Sampling Method [13]. Thanks to such a preprocessing of the scattered field data, the problem is recast into a linearized one, wherein the linearization has a much broader validity as compared to BA, since it implicitly takes the unknown targets into account.

As a consequence of the above, the adopted method allows tackling the inversion task in a computationally inexpensive fashion (in quasi-real-time) and free from false solutions, thus overcoming the aforementioned drawbacks. On the other side, the proposed method still relies on an approximation, so that its validity is in any case limited as compared to the full-wave iterative inversion schemes recalled above [8–10]. Nevertheless, results achieved in the canonical free space, as well as those presented in the following, confirm that the method is capable of succeeding also for scatterer far outside from the validity range of BA and that it can handle target usually handled via full-wave schemes [17, 18].

The paper is structured as follows. Section 2 recalls the electromagnetic scattering problem in presence of an embedding device. In Section 3 the Quantitative Linear Sampling Method is recalled and how the presence of the casing affects its implementation is described. Section 4 is devoted to a broad numerical analysis concerning different shaped cavities and different measurement strategies. Finally, in Section 5 some conclusions are given.

2. Statement of the Problem in a PEC Cavity

Let us consider the canonical 2D scalar inverse scattering problem in a PEC enclosure.

Let $D \subseteq \Re^2$ denote the domain enclosed in the casing, in which is embedded the cross section Σ of the unknown scatterers, whose properties, at the frequency ω, are related to those of the homogeneous host medium through the contrast function:

$$\chi(\underline{r}) = \frac{\epsilon_s(\underline{r})}{\epsilon_b(\underline{r})} - 1, \tag{1}$$

wherein $\underline{r}$ indicates the position of a generic point in D and ϵ_s and ϵ_b denote the complex permittivity of the scatterer and of the background medium, respectively.

The scatterers Σ are probed by a set of incident fields radiated by the transmitting antennas located at $\underline{r}_T$ on a closed curve Γ inside D, which can be a circle inscribed into the PEC enclosure, as well as a generic curve embedded into the casing. Receivers are located at the same positions of transmitters ($\underline{r}_R \equiv \underline{r}_T$).

By assuming the TM polarization for the electric field, the equations governing the scattering phenomenon in the considered geometry can be expressed in an integral form as

$$\begin{aligned} E_s(\underline{r}_T, \underline{r}_R) &= k_b^2 \int_D G(\underline{r}_R, \underline{r})\, \chi(\underline{r})\, E_t(\underline{r}, \underline{r}_T)\, d\underline{r} \\ &= \mathscr{A}_\Gamma[\chi E_t], \quad \underline{r}_T, \underline{r}_R \in \Gamma,\ \underline{r} \in D, \end{aligned} \tag{2}$$

$$\begin{aligned} &E_t(\underline{r}, \underline{r}_T) - E_i(\underline{r}, \underline{r}') \\ &\quad = k_b^2 \int_D G(\underline{r}, \underline{r}_T)\, \chi(\underline{r})\, E_t(\underline{r}, \underline{r}_T)\, d\underline{r} = \mathscr{A}_D[\chi E_t], \\ &\qquad \underline{r}, \underline{r}' \in D,\ \underline{r}_T \in \Gamma, \end{aligned} \tag{3}$$

wherein k_b is the wavenumber in the host medium, E_t, E_i, and E_s are the total, incident, and scattered field, respectively, and $G(\underline{r}, \underline{r}_T)$ is Green's function pertaining to the empty system, possibly filled with a homogeneous medium. The Green function is the kernel of the radiation operators $\mathscr{A}_\Gamma[\cdot] : L^2(D) \to L^2(\Gamma)$ and $\mathscr{A}_D[\cdot] : L^2(D) \to L^2(D)$ that relate

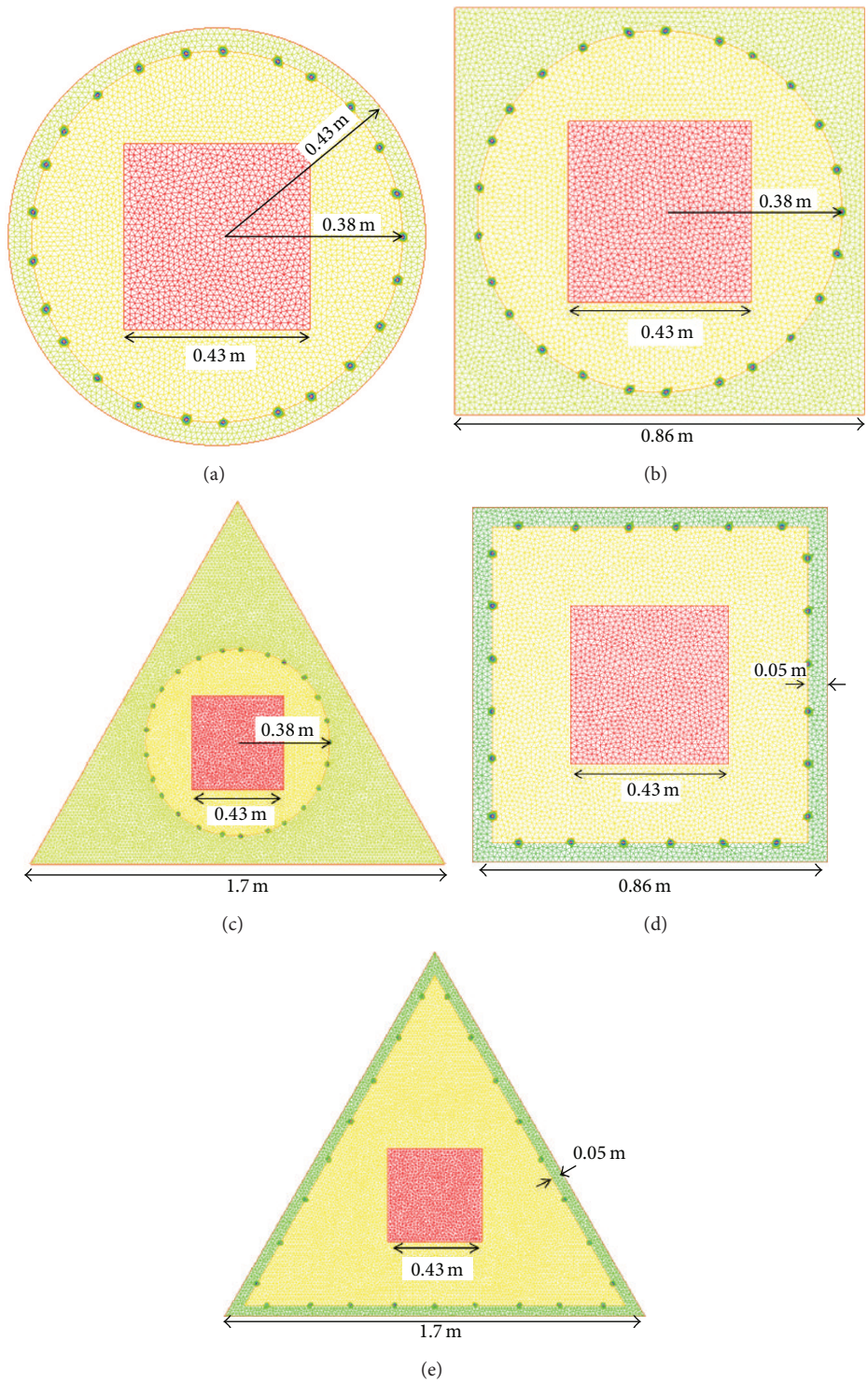

FIGURE 1: Considered measurement configurations: ((a), (b), and (c)) measurement configurations with probes on a circle located around the imaging domain (configuration A); ((d), (e)) measurement configurations with probes on lines parallel to the edges of the PEC at a distance equal to $\lambda_b/4$ (configuration B).

the contrast source $J(\underline{r}, \underline{r}_T) \propto \chi(\underline{r})E_t(\underline{r}, \underline{r}_T)$ in D to the field it radiates on Γ and in D, respectively.

In free space, that is, in absence of any enclosure, such Green's function is $G(\underline{r}, \underline{r}_T) = (-j/4)H_0^{(2)}(k_b|\underline{r} - \underline{r}_T|)$, $H_0^{(2)}$ being the zero-order second-kind Hankel function. In the cylindrical perfect electric conductor (PEC) embedding, it has been shown that such Green's function can be expressed as a single summation of Bessel functions [3, 19].

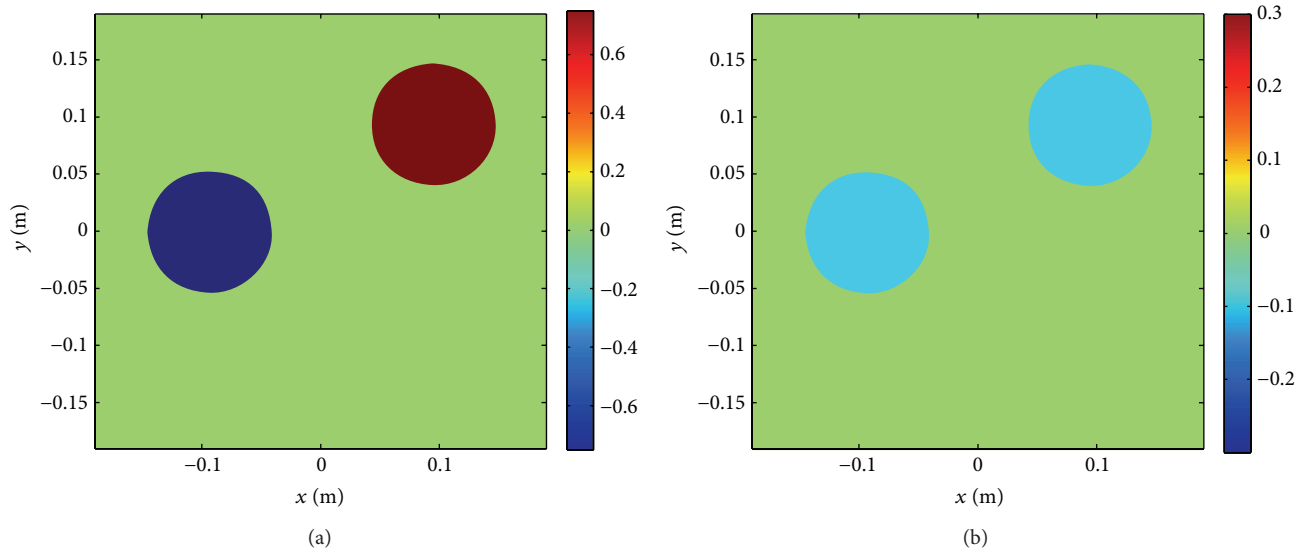

Figure 2: Example 1: reference profile. (a) Real and (b) imaginary parts of reference contrast function.

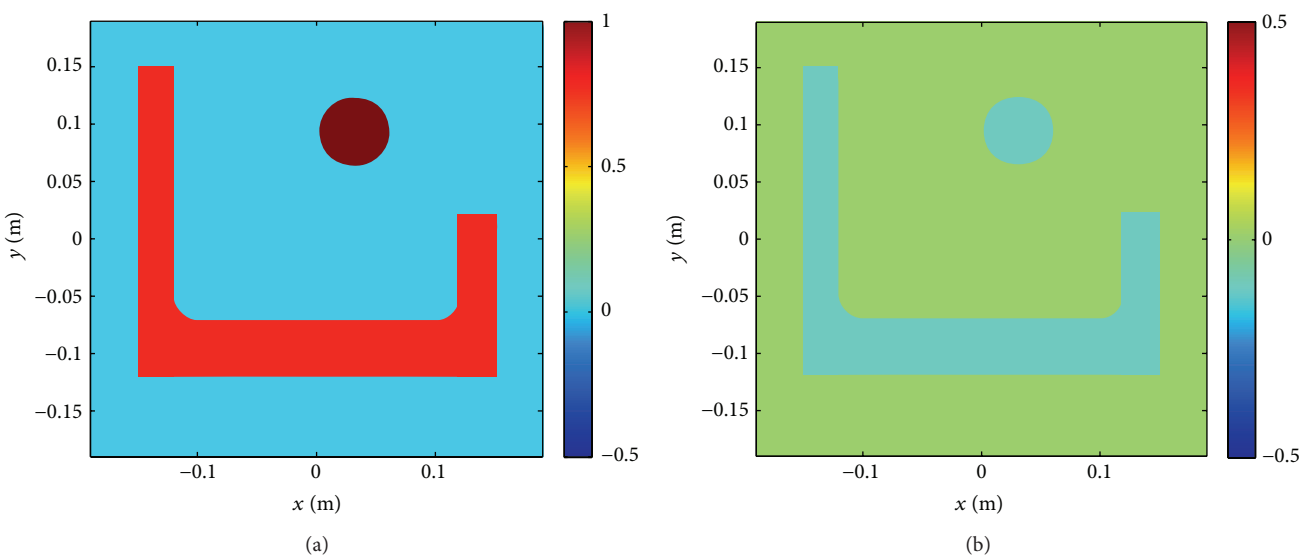

Figure 3: Example 2: reference profile. (a) Real and (b) imaginary parts of reference contrast function.

For noncanonical casing, instead, Green's function is not known in closed form, so its numerical evaluation is needed.

The inverse scattering problem at hand is then cast as retrieving the unknown contrast $\chi(\underline{r} \in D)$ from the measured scattered field $E_s(\underline{r}_R \in \Gamma)$ for known incident fields E_i.

3. A Simple Inversion Strategy: The Quantitative Linear Sampling Method

3.1. First Linear Step: The Linear Sampling Method. The LSM belongs to the class of qualitative reconstruction methods, as it provides an estimate of the targets support, but not its electric properties. The LSM requires solving an auxiliary linear inverse problem rather than the nonlinear one formulated through (2)-(3) [13]. With respect to the scenario described above, the auxiliary problem is cast as

$$\mathcal{F}[\xi] = \int_{\Gamma} E_s(\underline{r}_R, \underline{r}_T)\, \xi(\underline{r}_s, \underline{r}_T)\, d\underline{r}_T = G(\underline{r}_R, \underline{r}_s), \quad (4)$$

where $\underline{r}_s \in D$ denotes a point of an arbitrary grid that samples the region under test D, ξ is the unknown to be determined, and $\mathcal{F} : L^2(\Gamma) \rightarrow L^2(\Gamma)$ is the far field operator [13].

Due to compactness of $\mathcal{F}$, (4) corresponds to a linear ill-posed inverse problem [13]. Hence, a stable solution of (4) in the generic sampling point $\underline{r}_s \in D$ requires a regularization. Usually, this is done considering the Tikhonov regularization [20].

The estimated support is achieved by evaluating the energy (i.e., the L^2 norm) of $\xi, \forall \underline{r}_s \in D$, as this assumes

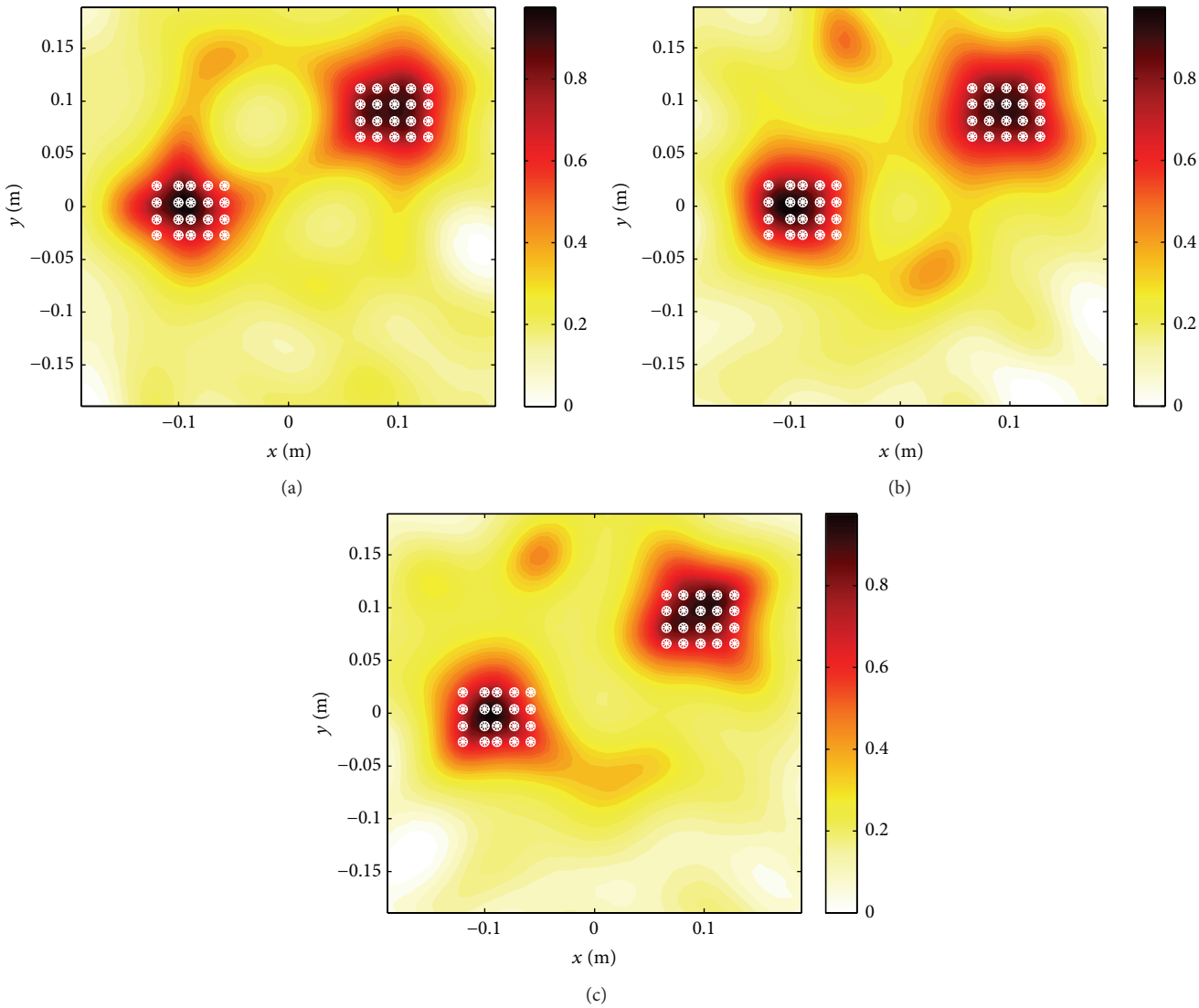

Figure 4: Example 1: LSM reconstructions by using measurement configuration A and corresponding pivot points. (a) Circular scanner, (b) square scanner, and (c) triangular scanner.

its lowest values in the points of the investigated region belonging to the target, while it diverges in points external to it [13]. Therefore, the support is simply determined by plotting the LSM indicator over D and associating the sampling points where the indicator is low to the unknown objects.

The explicit expression of the LSM indicator reads

$$\begin{aligned}\Upsilon(\underline{r}_s) &= \int_\Gamma \left|\xi(\underline{r}_s, \underline{r}_T)\right|^2 d\underline{r}_T \\ &= \sum_{n=1}^{\infty} \left(\frac{\lambda_n}{\lambda_n^2 + \alpha^2}\right)^2 \left\|\langle G(\underline{r}_R, \underline{r}_s), u_n(\underline{r}_R)\rangle\right\|_\Gamma^2,\end{aligned} \tag{5}$$

whose evaluation is computationally straightforward as it requires a single evaluation of the SVD of $\mathcal{F}(\{u_n, \lambda_n, v_n\})$. Moreover, the Tikhonov parameter can be determined only once for all sampling points [21–23]. In the examples of Section 4 this parameter is computed according to the physics based criterion introduced in [22].

3.2. Field Approximation. In order to better understand how the quantitative LSM (QLSM) works, let us note that

(1) by construction, $\mathcal{F}[\xi]$ represents a scattered field, as it is obtained through a linear combination of the measured data through the function $\xi(\underline{r}_s, \underline{r}_T)$;

(2) given the linearity of the relationship between incident fields and scattered ones, $\mathcal{F}[\xi]$ is the scattered field which is obtained on Γ when D is probed by means of the incident field:

$$\Psi_i(\underline{r}_s, \underline{r}) = \int_\Gamma \xi(\underline{r}_s, \underline{r}_T) E_i(\underline{r}, \underline{r}_T) d\underline{r}_T; \tag{6}$$

(3) in those points $\underline{r}_s \in D$ wherein the two sides of (4) match, the probing wave Ψ_i forces the targets to scatter

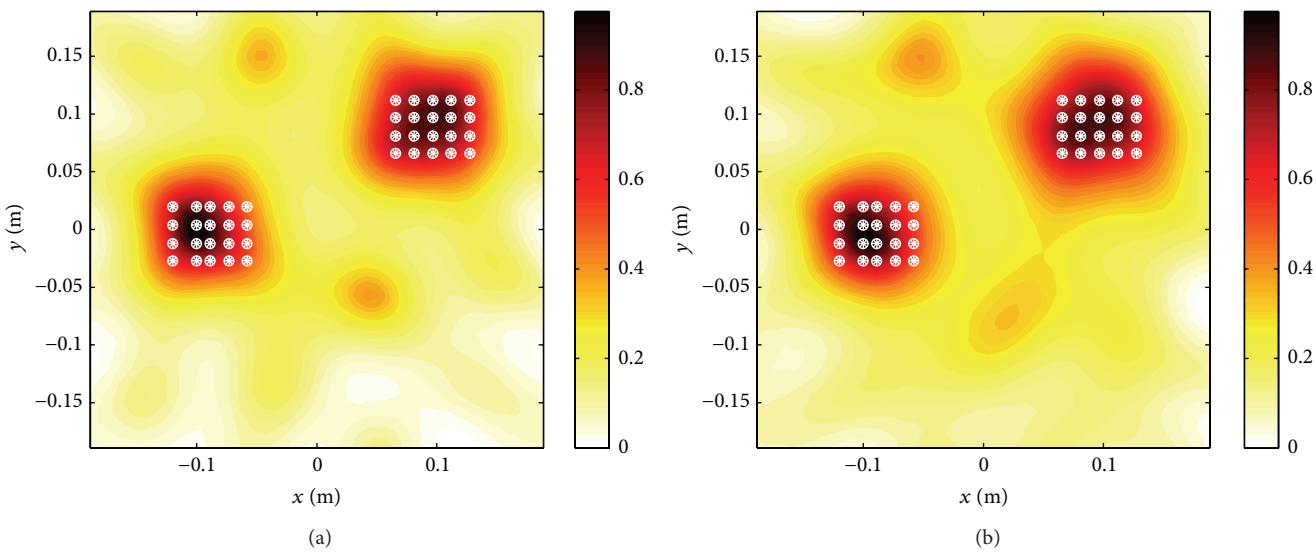

Figure 5: Example 1: LSM reconstructions by using measurement configuration B and corresponding pivot points. (a) Square scanner and (b) triangular scanner.

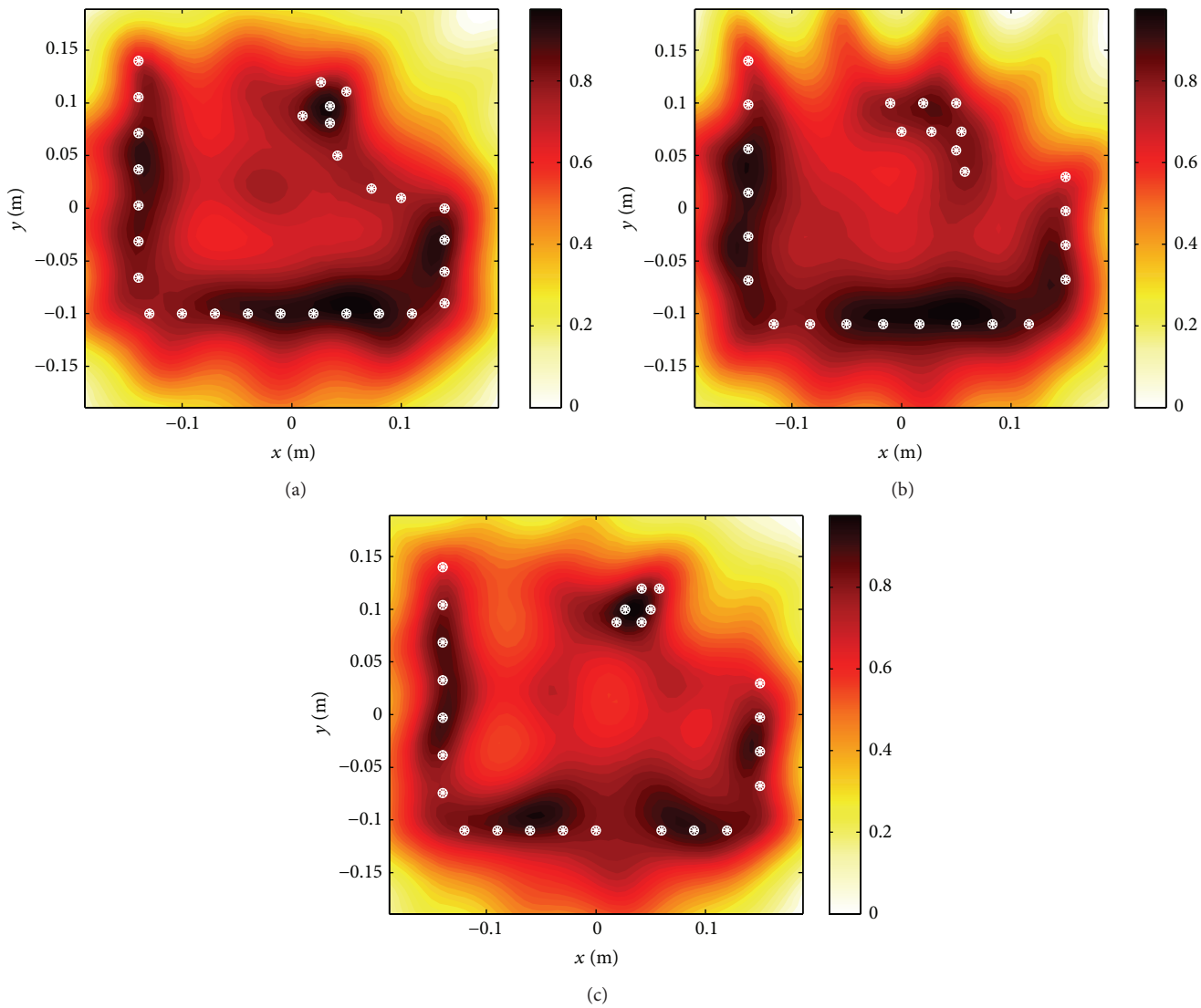

Figure 6: Example 2: LSM reconstructions by using measurement configuration A and corresponding pivot points. (a) Circular scanner, (b) square scanner, and (c) triangular scanner.

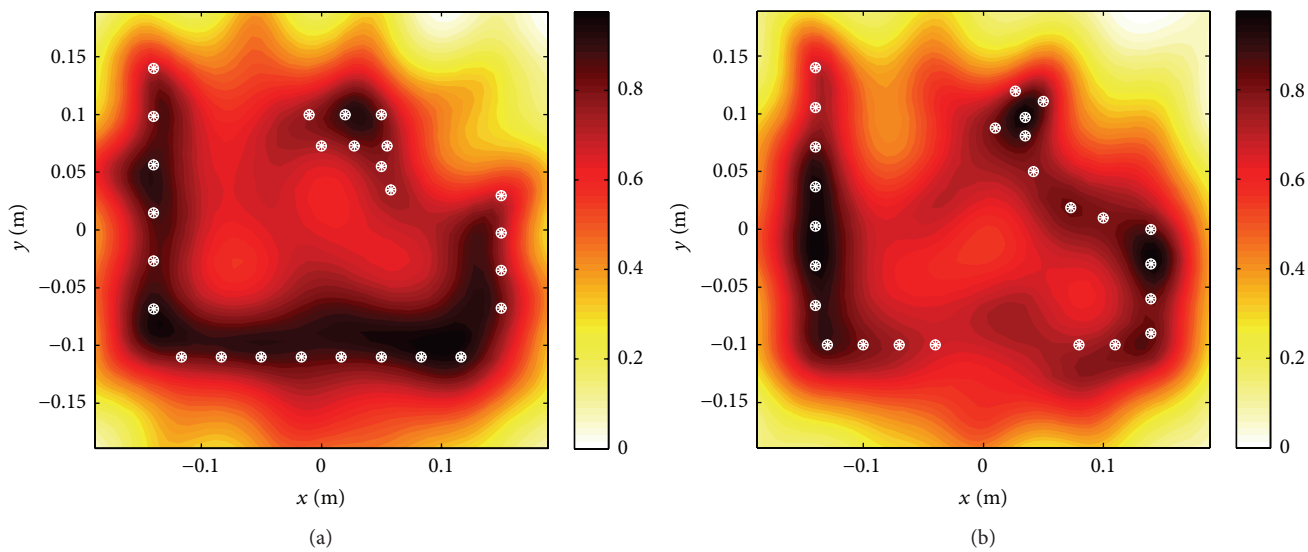

Figure 7: Example 2: LSM reconstructions by using measurement configuration B and corresponding pivot points. (a) Square scanner and (b) triangular scanner.

on Γ the field of a point source located in $\underline{r}_s$ (obviously in presence of the PEC).

These simple observations have an interesting implication. As a matter of fact, as long as the LSM equation (4) can be solved in the sampling point $\underline{r}_s$, ξ can be used to define an incident field whose corresponding scattered field is like the one radiated by a source centered on $\underline{r}_s$. Conversely, the incident wave (6) required to enforce this field depends on the scatterer under test through ξ. Clearly, this is the *opposite* of what happens in usual scattering experiments, where the scattered field changes with the scatterer, while the incident field is independent of it.

This concept can be exploited to cast a new approximation of the relationship between the contrast and the scattered fields. In particular, one can assume that when using Ψ_i as incident wave, the scattered field corresponds, in the *whole* space into the cavity and external to the sampling point at hand (rather than only on Γ as enforced by the LSM equation, this corresponds to analytically continuing the scattered field from Γ to Σ and then exploiting the continuity of the field's tangential component), to the field radiated by an elementary source located in $\underline{r}_s$. Accordingly, the total field will be

$$\Psi_t\left(\underline{r}_s, \underline{r}\right) = \Psi_i\left(\underline{r}_s, \underline{r}\right) + E_i\left(\underline{r}, rt\right), \quad \forall \underline{r} \neq \underline{r}_s. \tag{7}$$

By relying on the above concepts, the data-to-unknown relationship can be recast as

$$\begin{aligned} \mathscr{F}[\xi] &= \int_\Gamma E_s \xi\left(\underline{r}_s, \underline{r}_T\right) d\underline{r}_T \\ &= k_b^2 \int_D G\left(\underline{r}_T, \underline{r}'\right) \Psi_t\left(\underline{r}_s, \underline{r}'\right) \chi\left(\underline{r}'\right) dr' \\ &= \mathscr{A}_\Gamma\left[\chi \Psi_t\right], \end{aligned} \tag{8}$$

which provides a linear formulation of the inverse scattering problem, since the total field Ψ_t is assigned through (7).

With respect to the nature of the introduced approximation, it is worth remarking that the total field given in (7) is not the outcome of a straightforward linearization of the scattering equation (2). As a matter of fact, the linearization is achieved by replacing the unknown total field with a known (approximated) one, which takes the scatterer under test into account via the LSM preprocessing. As such, the exploited approximation is completely different from the Born one, in which the effect of the target on the total field is simply neglected.

3.3. Quantitative Linear Inversion. In this subsection, we recall the inversion method which relies on the LSM based approximation introduced in the previous subsection. To this end, let us first note that

(1) to achieve the new data equation (8) no additional measurements are necessary, as everything is done "virtually" via a rearrangement of the scattered fields ruled by LSM solution;

(2) by considering different sampling points for which the LSM equation is properly solved, it is possible to devise several "virtual" experiments, so as to rearrange the available multiview data into *multiple* virtual experiments.

Let us now assume that the original multiview multistatic configuration consists of N transmitters and M receivers.

The first step of the proposed method consists in the application of the LSM to the $M \times N$ data matrix E_s, to estimate the targets' shape through indicator (5).

Then, we select a subset of P sampling points belonging to the targets, $\underline{r}_1, \ldots, \underline{r}_P$. These points identify the virtual experiments. For each of them, we compute the approximated total field $\Psi_t(\underline{r}, \underline{r}_i)$, $i = 1, \ldots, P$, via (7) and then use these

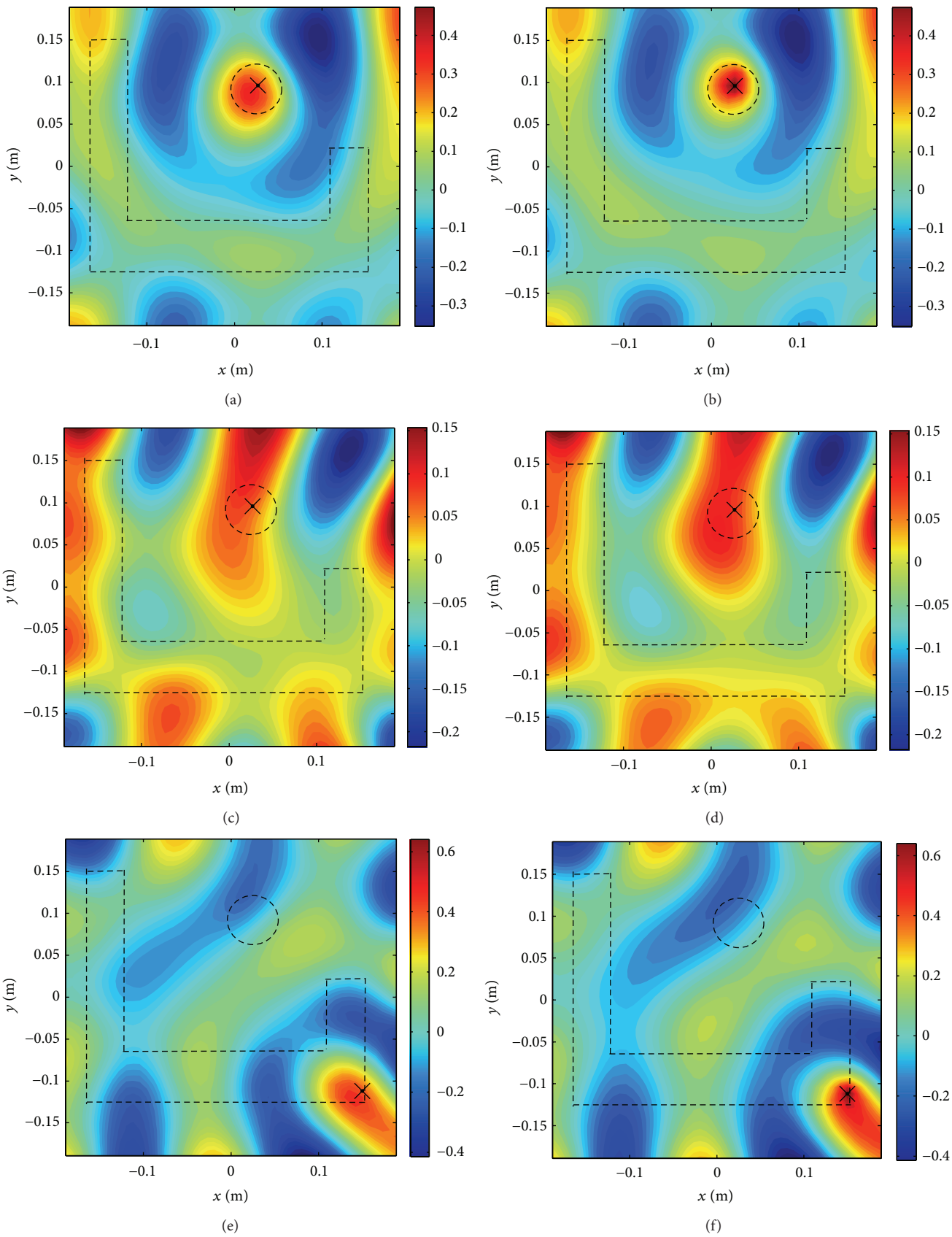

Figure 8: Continued.

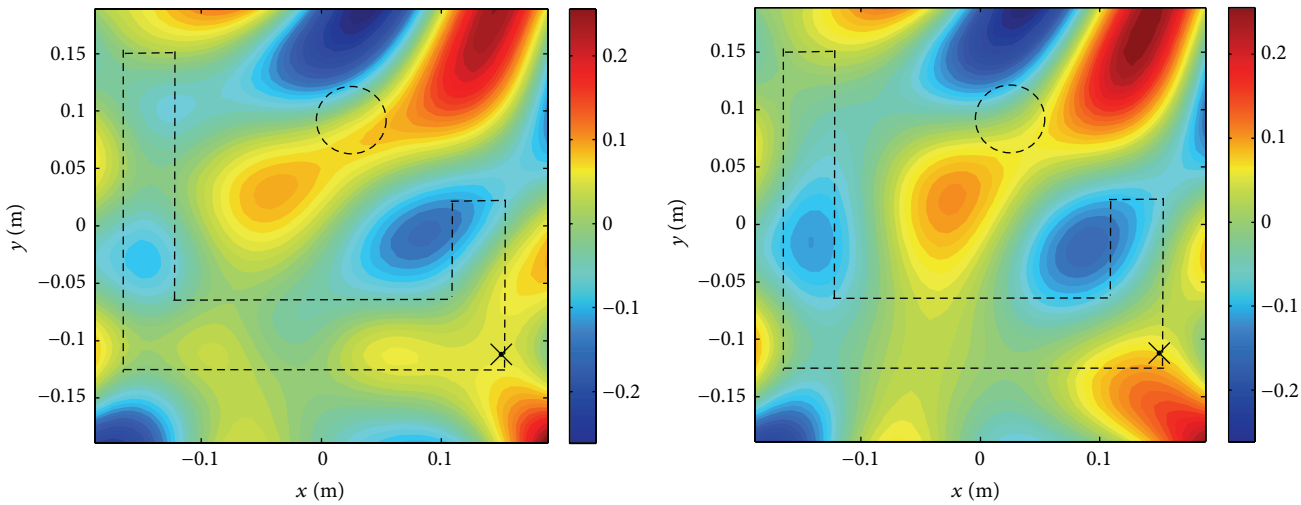

Figure 8: Performance assessment of the field approximation: comparison for the triangular cavity, example 2. ((a), (c)) Real and imaginary parts of total field in the minimum residual pivot point; ((b), (d)) real and imaginary parts of virtual field in the minimum residual pivot point; ((e), (g)) real and imaginary parts of total field in the maximum residual pivot point; ((f), (h)) real and imaginary parts of virtual field in the maximum residual pivot point.

fields to build the data-to-unknown matrix equation that corresponds to the considered multiple virtual experiments:

$$\mathbf{L}\mathbf{c} = \mathbf{f}_{\Gamma}. \tag{9}$$

In (9), assuming that the domain under test D has been discretized into N_c cells,

$$\mathbf{c} = [\chi_1 \ \cdots \ \chi_k \ \cdots \ \chi_{N_c}]^T \tag{10}$$

is the $N_c \times 1$ matrix containing the values of the unknown contrast in the discretized investigation domain, with ^{T} denoting the matrix transposition,

$$\mathbf{f}_{\Gamma} = [f_1 \ \cdots \ f_i \ \cdots \ f_P]^T \tag{11}$$

is the $(P \times M) \times 1$ matrix in which each element f_i is a $M \times 1$ matrix containing the samples of the scattered field for the ith virtual experiment, $\mathcal{F}[\xi(\underline{r}_i)]$, and

$$\mathbf{L} = \begin{bmatrix} l_{11,1} & \cdots & l_{11,N_c} \\ \vdots & \ddots & \vdots \\ l_{1M,1} & \cdots & l_{1M,N_c} \\ \vdots & \ddots & \vdots \\ l_{PM,1} & \cdots & l_{PM,N_c} \end{bmatrix} \tag{12}$$

is $(P \times M) \times N_c$ matrix that represents the discretization of the approximated data equations for the considered multiple virtual experiments, with $l_{ij,k} = \Psi_t(\underline{r}_i, \underline{r}_k) G(\underline{r}_j, \underline{r}_k)$.

By denoting with $\{\mathbf{W}, \mathbf{S}, \mathbf{Z}\}$ the SVD of $\mathbf{L}$, (9) can be solved via truncated SVD (TSVD) [20], thus achieving the expression for the estimated unknown contrast:

$$\chi_k = \sum_{n=1}^{N_T} \frac{1}{\sigma_n} \langle \mathbf{f}_{\Gamma}, \mathbf{w}_{\mathbf{n}} \rangle z_{nk}, \tag{13}$$

wherein $\mathbf{w}_{\mathbf{n}}$ is the nth column of $\mathbf{W}$, z_{nk} is the kth element of the nth column of $\mathbf{Z}^T$, and σ_n is the nth element on the diagonal of $\mathbf{S}$.

The truncation index N_T, which is the regularization parameter of this inversion scheme, is determined to get a tradeoff between the accuracy and the stability of the reconstruction.

4. Numerical Analysis

In this section we present some numerical examples in order to assess the performance of the QLSM, recalled in previous section, in noncanonical embedding systems. The case is supposed to be a perfectly electric conductor (PEC), filled by a matching medium whose electromagnetic features are $\epsilon_b = 2.5$ and $\sigma_b = 10$ mS/m. Three different kinds of metallic enclosures have been considered: a circular cavity, a square, and a triangular one. In these systems the imaging domain is represented by a square whose size is equal to 0.38 m (about 2λ). The working frequency has been fixed at 1 GHz and the probes have been located in two different configurations.

(i) *Measurement configuration A:* the probes are equally spaced on a circle surrounding the imaging domain, whose radius is equal to 0.38 m.

(ii) *Measurement configuration B:* the probes are equally spaced along the edges of the cavity at a distance equal

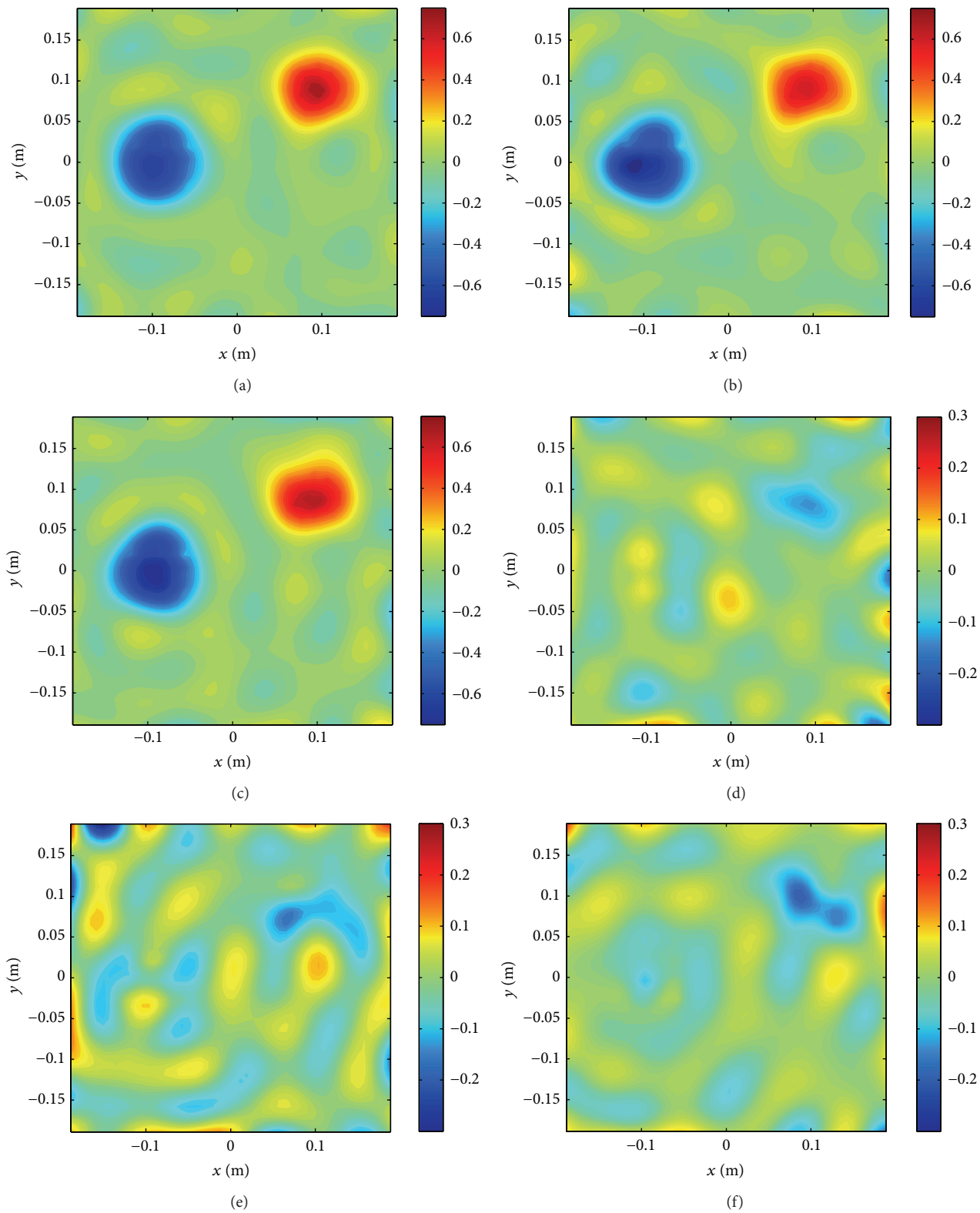

Figure 9: Example 1: QLSM reconstructions by using measurement configuration A. ((a), (d)) Real and imaginary parts of retrieved profiles in a circular scanner; ((b), (e)) real and imaginary parts of retrieved profiles in a square scanner; ((c), (f)) real and imaginary parts of retrieved profiles in a triangular scanner.

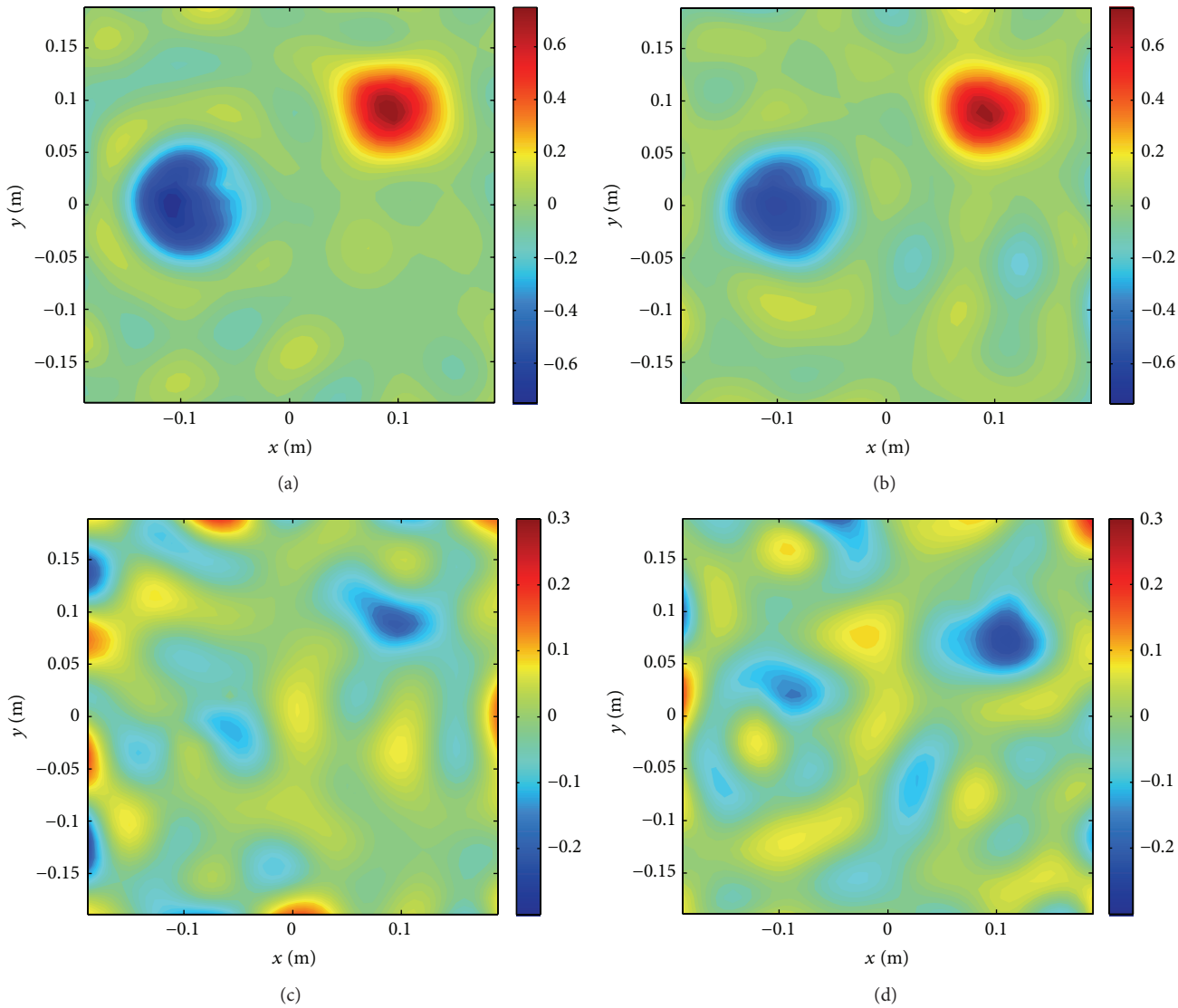

Figure 10: Example 1: QLSM reconstructions by using measurement configuration B. ((a), (c)) Real and imaginary parts of retrieved profiles in a square scanner; ((b), (d)) real and imaginary parts of retrieved profiles in a triangular scanner.

to $\lambda_b/4$ (about 4.75 cm), as suggested by the analysis in [5].

The transmitter/receiver antennas are infinite-length filamentary sources located inside the cavity. When an antenna is transmitting, all the others are in receiving mode.

Figure 1 shows the two configurations for the considered kinds of enclosures, as well as the size of the metallic cases.

It is important to underline that the number of probes has been chosen by relying on the degrees of freedom theory [24, 25], and for the following examples, it has been fixed at 25 transmitters (and accordingly 24 receivers per each view).

In each example, two different discretization grids for the generation of data and for the inversion procedure have been adopted, so as to avoid the so-called inverse crime. In particular, the data and Green's functions were generated by using a nodal grid, produced by means of the mesh generator GiD, which is available online [26], while the inversion procedures have been carried out on rectangular grids. Note that Green's function of the cavity at hand is exploited throughout the inversion step, so a "migration" from the nodal space to a standard rectangular grid is performed [9].

All numerical examples have been performed on a standard laptop with a 2.20 GHz Intel Core Duo CPU, 4 GB RAM, and equipped with a 64-bit Microsoft Windows 7 OS, taking computational time lower than one minute per each scenario.

For each configuration and enclosure, two different examples have been considered, as detailed in the following.

(1) In the first example, two circular scatterers, each one of radius equal to $r = 4.7$ cm and center equal to $c_1 = (9.4, 9.4)$ cm and $c_2 = (-9.4, 0)$ cm, have been considered. The two objects have permittivity values equal to $\epsilon_1 = 4.36$ and $\epsilon_2 = 0.616$ and conductivities $\sigma_1 = 0.0152$ S/m and $\sigma_2 = 0.0227$ S/m. The real and

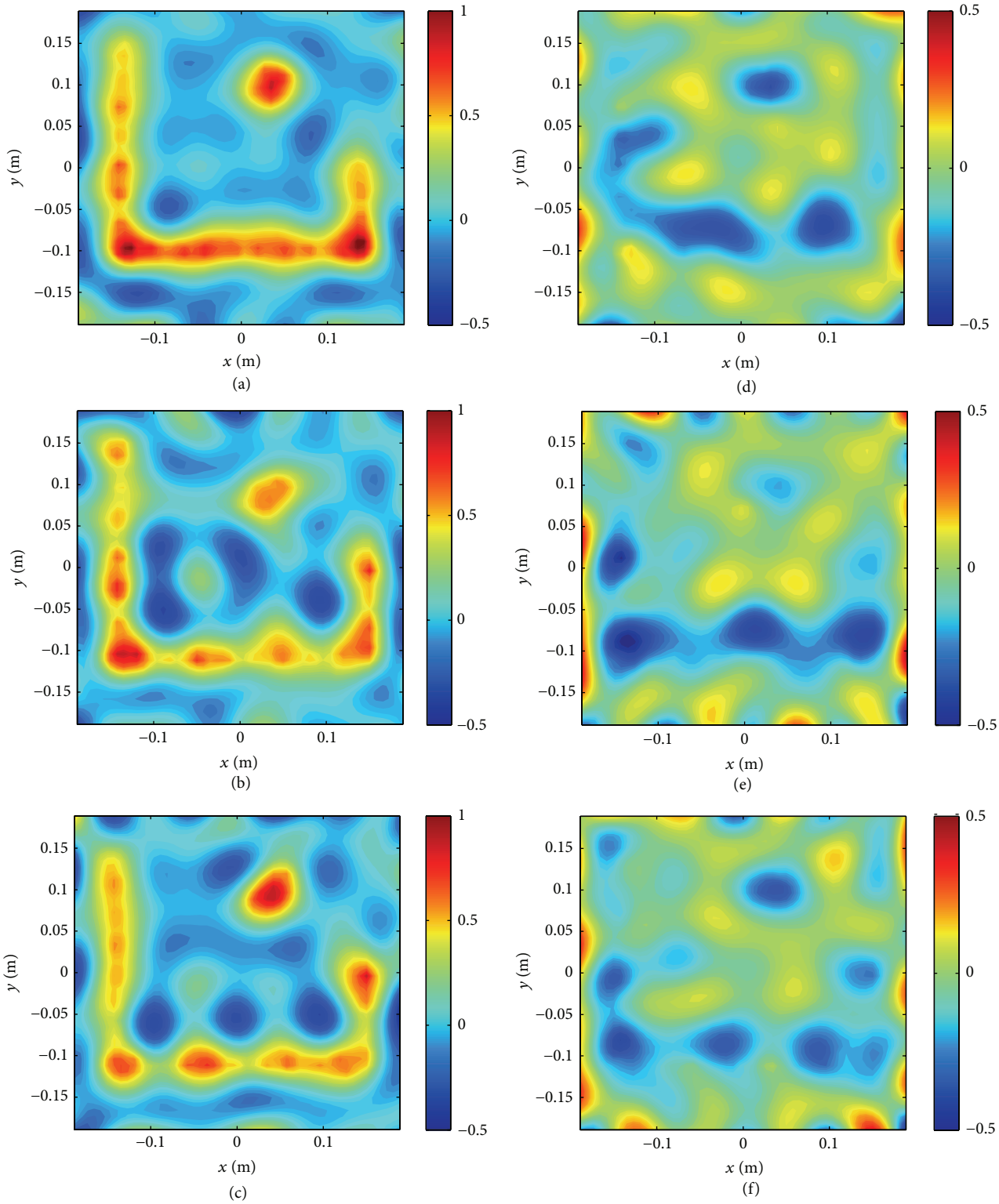

Figure 11: Example 2: QLSM reconstructions by using measurement configuration A. ((a), (d)) Real and imaginary parts of retrieved profiles in a circular scanner; ((b), (e)) real and imaginary parts of retrieved profiles in a square scanner; ((c), (f)) real and imaginary parts of retrieved profiles in a triangular scanner.

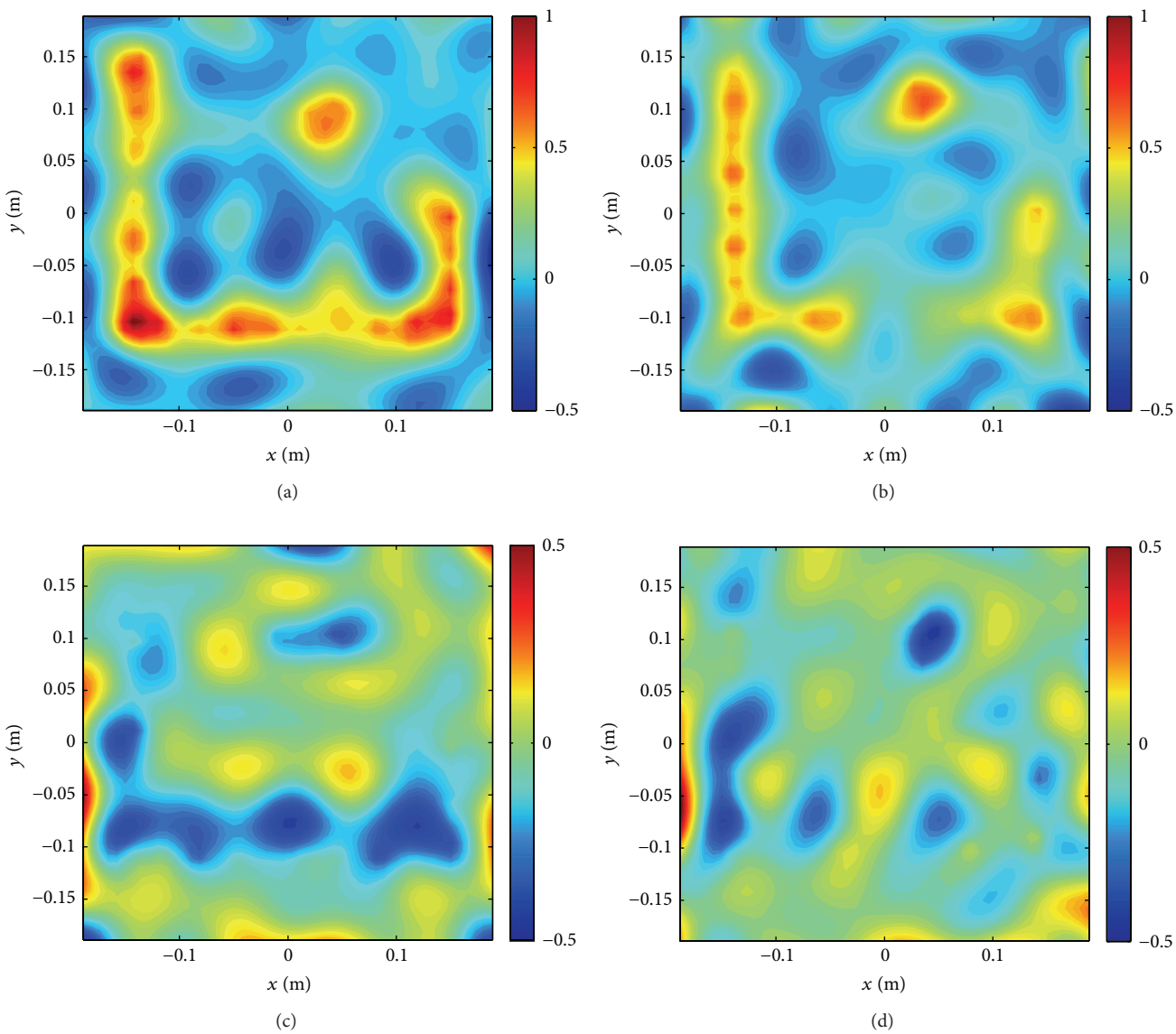

Figure 12: Example 2: QLSM reconstructions by using measurement configuration B. ((a), (c)) Real and imaginary parts of retrieved profiles in a square scanner; ((b), (d)) real and imaginary parts of retrieved profiles in a triangular scanner.

imaginary parts of the corresponding contrast profile are depicted in Figure 2.

(2) In the second example, the reference scenario consists of two objects: one is L-shaped object with $\epsilon_1 = 0.616$ and $\sigma_1 = 0.0227$ S/m, while the second one is a circular target located in the imaging domain at $c_2 = (9.4, 3.13)$ cm and radius $r_2 = 3$ cm, with permittivity $\epsilon_2 = 5$ and conductivity $\sigma_2 = 0.024$ S/m, respectively.

Figure 3 shows the corresponding reference contrast function.

All the data employed for the inversion procedure have been corrupted by additive white Gaussian noise, with a SNR value equal to 20 dB.

The performance of the inversion method is quantitatively assessed by means of the normalized mean square error on the contrast function defined as

$$\text{err} = \frac{\left\|\hat{\chi} - \chi_{\text{true}}\right\|^2}{\left\|\chi_{\text{true}}\right\|^2}. \tag{14}$$

4.1. Linear Sampling Method: An Estimation of Targets Support. As mentioned in Section 3.1, the first step of the investigated inversion strategy consists of performing the Linear Sampling Method (LSM) and retrieving the support of the targets inside the imaging domain. This has been done for all the configurations and the examples previously described. In Figures 4, 5, 6, and 7 the obtained maps of the LSM indicators are shown. Then, based on the LSM reconstructions, one

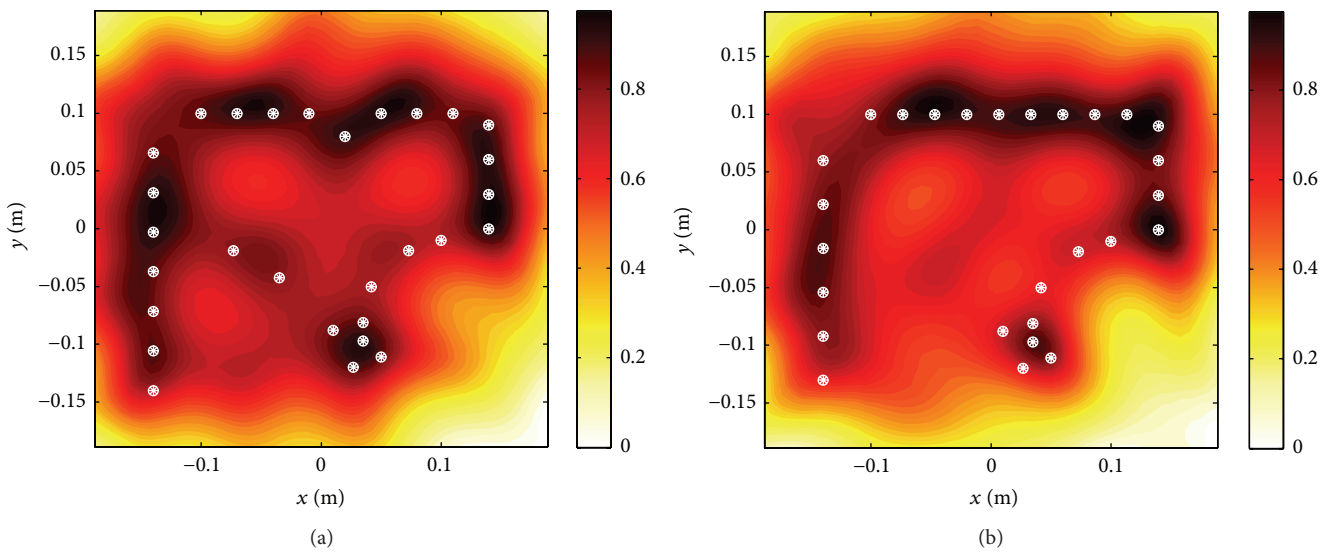

Figure 13: LSM indicator for flipped example 2 in a triangular cavity. (a) Measurement configuration A and (b) measurement configuration B.

can identify a number of "sampling points" or "pivot points" inside the objects, in which we can assume that the far field equation is accurately verified [17]. In Figures 4, 5, 6, and 7, the selected sampling points are represented by the white circles and their number is chosen approximately equal to the number of probes [17].

4.2. Validation of the Field's Approximation. As detailed in Section 3.2, a key idea on which the QLSM relies is represented by the possibility of accurately approximating the field in the overall investigated domain, by means of a proper recombination of the measured scattered fields. This is done by synthesizing a number of virtual experiments in the previously selected sampling points.

In order to investigate the fidelity of field approximation we can get by means of virtual experiments, among all the selected pivot points and for each example and measurement configuration, we have considered the two virtual experiments pertaining to the sampling points in which the residual of the far field equation is minimum and maximum, respectively. In this way, we analyze the accuracy of the field approximation in the best and in the worst case.

As an example, in Figure 8 is shown the comparison between the actual total field (computed by means of a FEM based forward solver) and the virtual one for example 2 in a triangular cavity by using a measurement configuration B, which, according to the LSM reconstructions reported above, is one of the most critical cases.

As expected and predicted in Section 3.2, there is a good matching in the overall domain, but for $\underline{r} \equiv \underline{r}_s$ and the mean square errors evaluated for the minimum and maximum residual pivot points are 0.06 and 0.13, respectively.

Similar results have been obtained in all the examples and are herein omitted for the sake of brevity. However, the mean square error of the field approximation is below 10% for all the analyzed cases.

Table 1: Ideal reconstruction error.

	Example 1			Example 2		
	CC	CQ	CT	CC	CQ	CT
Config. A	0.27	0.29	0.25	0.22	0.35	0.29
Config. B		0.24	0.30		0.30	0.38

4.3. Quantitative Recovery. Before presenting quantitative reconstructions obtained by means of the QLSM, let us observe that the efficacy of the method depends on the accuracy with which we are able to approximate the field inside the investigated domain. Ideally, if we assume the exact knowledge of the field's distribution, no approximation is needed and the linear inversion of (9) (where each element of the matrix $\mathbf{L}$ is equal to $l_{ij,k} = E_t(\underline{r}_i, \underline{r}_k)G(\underline{r}_j, \underline{r}_k)$, that is, replacing the virtual total field with the exact one), provides the best achievable result (by means of a linear inversion). Such a "best" reconstruction represents a low-pass filtered version of the actual profile. Accordingly, for all the considered examples we have performed the linear inversion of the "exact" operator $\mathbf{L}$ and the obtained reconstruction errors are reported in Table 1. These values represent the minimum errors that we can get by means of a linear processing of the data and, as such, they represent a sort of benchmark for our performance assessment.

Hence, starting from the the support estimation presented in the previous subsection, we selected 40 sampling points for the first example and about 24 for the second one. Then we have built and inverted the tomographic operator $\mathbf{L}$ in (9) (a threshold equal to −10 dB has been applied to the singular value decomposition (SVD) of $\mathbf{L}$). Results are shown in Figures 9, 10, 11, and 12 and the corresponding reconstruction errors in Table 2.

As a first comment, let us again stress that the reconstructions obtained by using QLSM strongly depend on the LSM

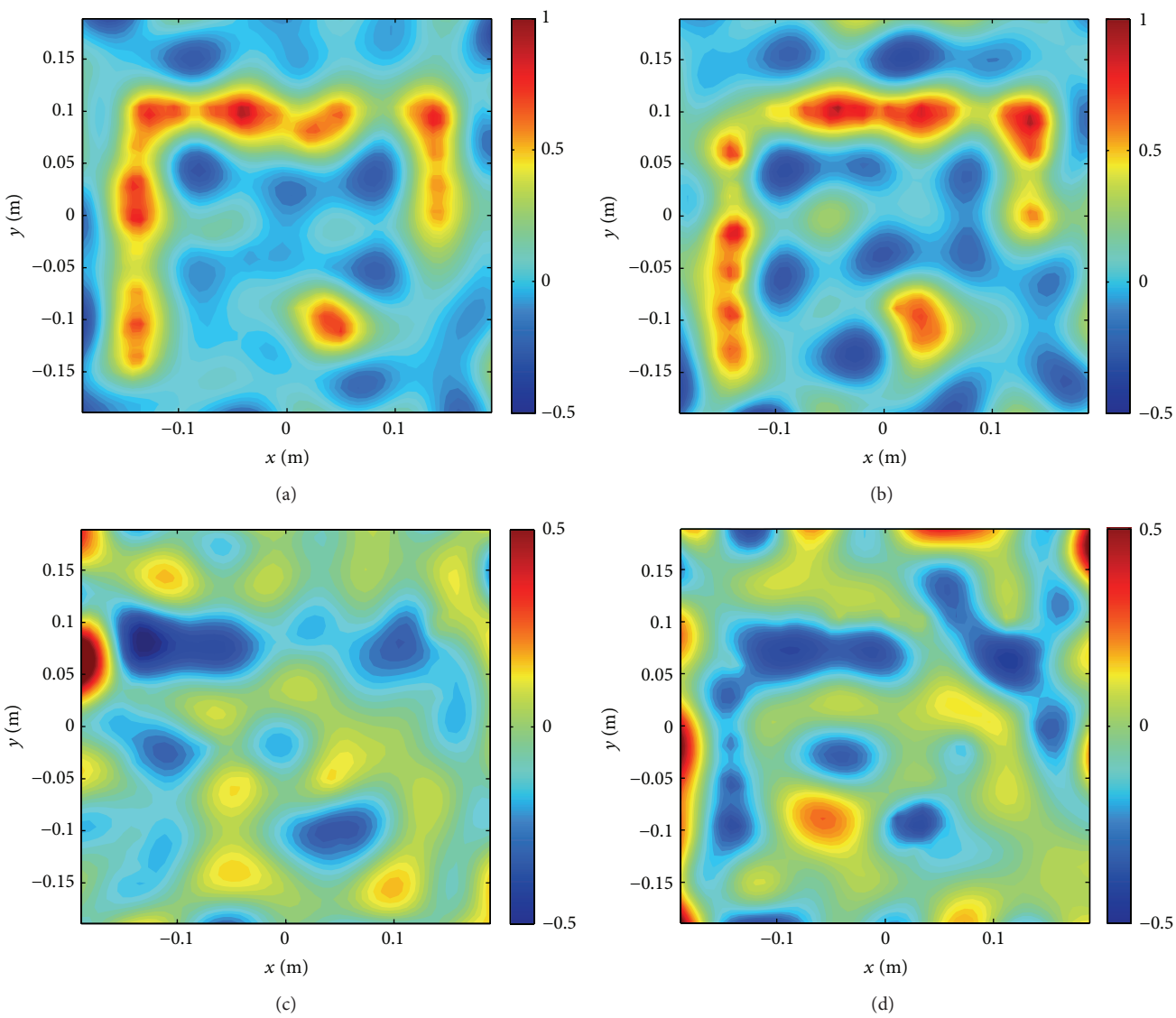

Figure 14: Example 2 with flipped scatterers: QLSM reconstructions in a triangular enclosure. ((a), (c)) Real and imaginary parts of retrieved profiles in measurement configuration A; err = 0.35. ((b), (d)) Real and imaginary parts of retrieved profiles in measurement configuration B; err = 0.45.

Table 2: Reconstruction error.

	Example 1			Example 2		
	CC	CQ	CT	CC	CQ	CT
Config. A	0.28	0.32	0.26	0.29	0.46	0.48
Config. B		0.28	0.32		0.43	0.44

indicator: therefore, the better the LSM works, the better the QLSM recoveries will be (if appropriate number of sampling points is chosen).

As can be seen, satisfactory results have been achieved, as demonstrated also by the fact that the reconstruction errors in Table 2 only slightly differ from the ideal ones (reported in Table 1). On the other hand, it is worth noting that, in example 2, the obtained result (but also the support indicator) strongly depends on the kind of enclosure and it is particularly worsened in the triangular casing. This may be due to to the fact that, in this embedding system, the presence of acute corners may cause multiple reflections between the borders of the cavity, resulting in trapping the field and in a loss of energy that does not come back to receiving antennas, especially for the measurement configuration B, in which case the probes are closer to the corners rather than in measurement configuration A. This effect is not observed in example 1 because of the position and the size of the targets, which result far from the corners of the cavity.

To corroborate this ansatz, we have repeated example 2 "flipping" the object into the cavity. As shown in Figure 13, in this case the LSM indicator works better, managing to retrieve the targets support also in the most critical situation

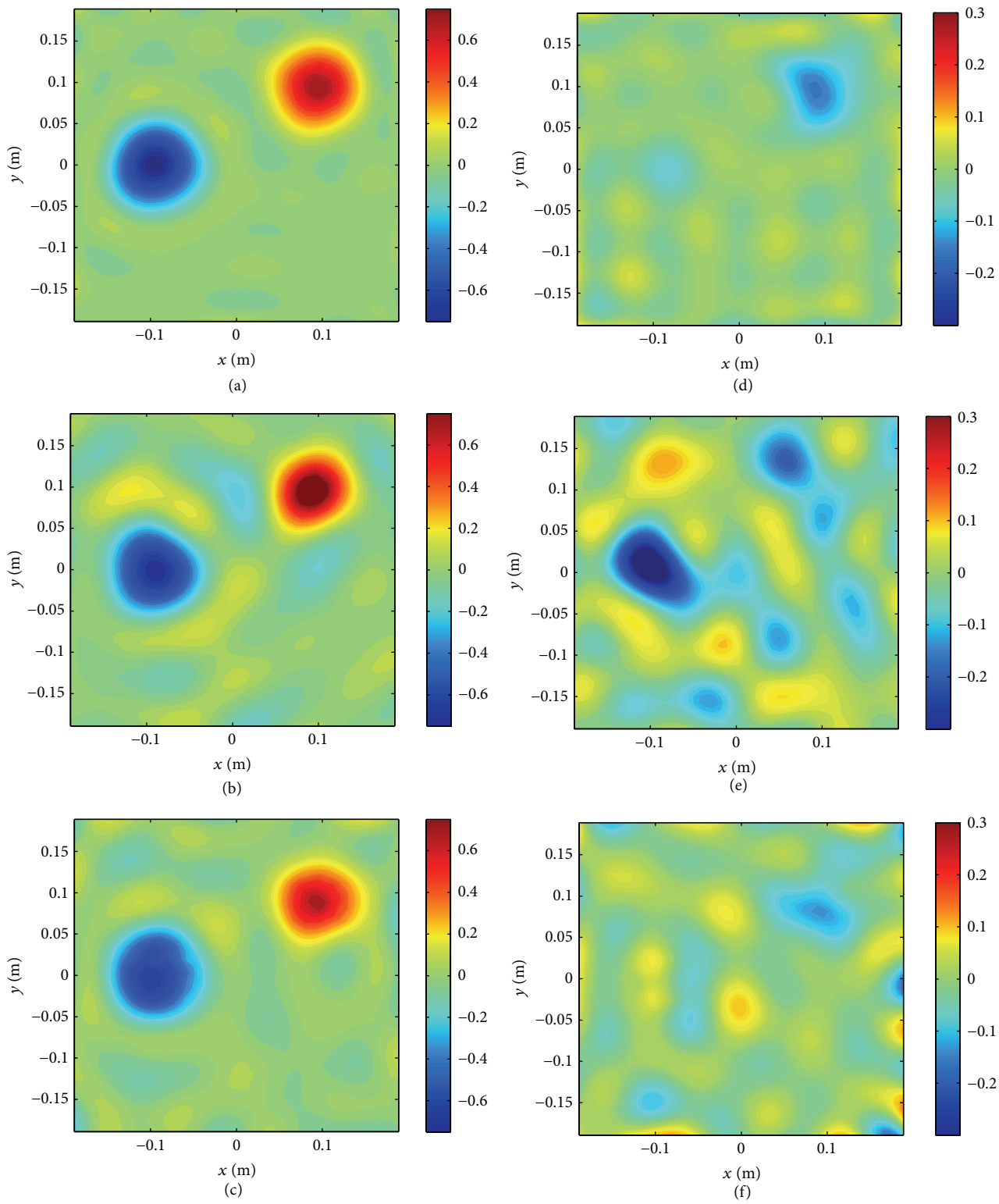

Figure 15: Example 1: reconstructions in the circular cavity. ((a), (d)) Real and imaginary parts of retrieved contrast function assuming the "exact" scattering operator; ((b), (e)) real and imaginary parts of retrieved contrast function by measn of the DBIM; ((c), (f)) real and imaginary parts of retrieved contrast function via QLSM.

of measurement configuration B. Accordingly, also the quantitative reconstruction shown in Figure 14 appears improved reaching reconstruction errors lower than the corresponding cases previously considered.

Finally, a nonlinear inversion has been performed as well, by adopting the Distorted Born Iterative Method scheme [27]. For brevity, in Figure 15 we show only the case of example 1 in a circular cavity and we report the reconstructions obtained by inverting the "exact" linear operator **L** (panels (a), (d)) and the DBIM reconstructions (panels (b), (e)) and we report again the QLSM reconstructions (panels (c), (f)) already shown in Figure 9.

As can be seen, comparable results are obtained via DBIM and via QLSM and, as expected, in both cases such results are worse than the benchmark. However, the contrast function retrieved by means of the DBIM is slightly overestimated and this brings to a slightly larger reconstruction error err = 0.31 (this value must be compared to the reconstruction error reported in Table 2, first column). This occurrence is due to not optimized choices of the regularization parameters in the nonlinear inversion (as, e.g., the number of the DBIM iterations).

5. Conclusions

In this paper we have presented and assessed a simple and effective inversion strategy for quantitative microwave imaging in noncanonical PEC embedded systems. As a matter of fact, the presence of a confining structure is common to several applications of microwave imaging, as it allows shielding the imaging domain from environmental noise as well as containing a possible matching medium needed for coupling purposes. On the other hand, the embedded systems require a proper modeling of the scenario under test to make the processing of the acquired data reliable.

In this frame, we have generalized a recently proposed quantitative inversion strategy based on the LSM to the cases of PEC enclosures of arbitrary shapes. The main advantages of the QLSM stand in its simplicity, fastness, and effectiveness in a broad class of scenarios. The presence of the PEC enclosure has been modeled by exploiting a 2D TM full-wave forward based on the Finite Element Method (FEM), not only for the simulation of synthetic data, but also (and more important) to compute Green's function of the actual system at hand, which is not known in analytic form but for the case of a circular cross section PEC embedding.

The performed numerical analysis confirmed the effectiveness of the QLSM as a way to reliable quantitative recovery strategy, also against complex scenarios and in presence of not canonical shaped enclosures. Future work will be concerned with the range of applicability of the method (with respect to the maximum contrast which can be reliably recovered), as already carried out in free space [28].

Conflict of Interests

The authors declare that there is no conflict of interests regarding the publication of this paper.

References

[1] M. Pastorino, Ed., *EM Applications of Microwave Imaging*, John Wiley & Sons, Hoboken, NJ, USA, 2010.

[2] P. M. Meaney, M. W. Fanning, T. Raynolds et al., "Initial clinical experience with microwave breast imaging in women with normal mammography," *Academic Radiology*, vol. 14, no. 2, pp. 207–218, 2007.

[3] J. M. Geffrin, *EM Imagerie microonde: Etude dun scanner a 434 MHz pour des applications biomedicales [Ph.D. thesis]*, University of Paris XI, Orsay, France, 1995.

[4] C. Gilmore, P. Mojabi, A. Zakaria et al., "A wideband microwave tomography system with a novel frequency selection procedure," *IEEE Transactions on Biomedical Engineering*, vol. 57, no. 4, pp. 894–904, 2010.

[5] L. Crocco and A. Litman, "On embedded microwave imaging systems: retrievable information and design guidelines," *Inverse Problems*, vol. 25, no. 6, Article ID 065001, 17 pages, 2009.

[6] C. Gilmore and J. LoVetri, "Enhancement of microwave tomography through the use of electrically conducting enclosures," *Inverse Problems*, vol. 24, no. 3, Article ID 035008, 21 pages, 2008.

[7] J. Jin, *The Finite Element Method in Electromagnetics*, Wiley-Interscience, Hoboken, NJ, USA, 2nd edition, 2002.

[8] R. Lencrerot, A. Litman, H. Tortel, and J.-M. Geffrin, "Measurement strategies for a confined microwave circular scanner," *Inverse Problems in Science and Engineering*, vol. 17, no. 6, pp. 787–802, 2009.

[9] A. Zakaria, C. Gilmore, and J. LoVetri, "Finite-element contrast source inversion method for microwave imaging," *Inverse Problems. An International Journal on the Theory and Practice of Inverse Problems, Inverse Methods and Computerized Inversion of Data*, vol. 26, no. 11, Article ID 115010, 115010, 21 pages, 2010.

[10] E. A. Attardo, G. Vecchi, and L. Crocco, "Contrast source extended born inversion in noncanonical scenarios via fem modeling," *IEEE Transactions on Antennas and Propagation*, vol. 62, no. 9, pp. 4674–4685, 2014.

[11] R. Scapaticci, O. M. Bucci, I. Catapano, and L. Crocco, "Differential microwave imaging for brain stroke followup," *International Journal of Antennas and Propagation*, vol. 2014, Article ID 312528, 11 pages, 2014.

[12] G. Bellizzi, O. M. Bucci, and I. Catapano, "Microwave cancer imaging exploiting magnetic nanoparticles as contrast agent," *IEEE Transactions on Biomedical Engineering*, vol. 58, no. 9, pp. 2528–2536, 2011.

[13] D. Colton, H. Haddar, and M. Piana, "The linear sampling method in inverse electromagnetic scattering theory," *Inverse Problems*, vol. 19, no. 6, pp. S105–S137, 2003.

[14] A. J. Devaney, E. A. Marengo, and F. K. Gruber, "Time-reversal-based imaging and inverse scattering of multiply scattering point targets," *The Journal of the Acoustical Society of America*, vol. 118, no. 5, pp. 3129–3138, 2005.

[15] A. Kirsch and N. Grinberg, *The Factorization Method for Inverse Problems*, Oxford Lecture Series in Mathematics and Its Applications, Oxford University Press, Oxford, UK, 2008.

[16] M. Slaney, A. C. Kak, and L. E. Larsen, "Limitations of imaging with first-order diffraction tomography," *IEEE Transactions on Microwave Theory and Techniques*, vol. 32, no. 8, pp. 860–874, 1984.

[17] L. Crocco, I. Catapano, L. Di Donato, and T. Isernia, "The linear sampling method as a way to quantitative inverse scattering,"

Institute of Electrical and Electronics Engineers. Transactions on Antennas and Propagation, vol. 60, no. 4, pp. 1844–1853, 2012.

[18] L. Di Donato, R. Palmeri, G. Sorbello, T. Isernia, and L. Crocco, "Assessing the capabilities of a new linear inversion method for quantitative microwave imaging," *International Journal of Antennas and Propagation*, In press.

[19] P. M. Van den Berg and J. T. Fokkema, "Removal of undesired wavefields related to the casing of a microwave scanner," *IEEE Transactions on Microwave Theory and Techniques*, vol. 51, no. 1, pp. 187–192, 2003.

[20] M. Bertero and P. Boccacci, Eds., *Introduction to Inverse Problems in Imaging*, Institute of Physics Publishing, Bristol, UK, 1998.

[21] I. Catapano, L. Crocco, and T. Isernia, "On simple methods for shape reconstruction of unknown scatterers," *IEEE Transactions on Antennas and Propagation*, vol. 55, no. 5, pp. 1431–1436, 2007.

[22] I. Catapano and L. Crocco, "An imaging method for concealed targets," *IEEE Transactions on Geoscience and Remote Sensing*, vol. 47, no. 5, pp. 1301–1309, 2009.

[23] M. Brignone, G. Bozza, R. Aramini, M. Pastorino, and M. Piana, "A fully no-sampling formulation of the linear sampling method for three-dimensional inverse electromagnetic scattering problems," *Inverse Problems*, vol. 25, no. 1, Article ID 015014, 2009.

[24] O. M. Bucci and G. Franceschetti, "On the spatial bandwidth of scattered fields," *IEEE Transactions on Antennas and Propagation*, vol. 35, no. 12, pp. 1445–1455, 1987.

[25] O. M. Bucci and G. Franceschetti, "On the degrees of freedom of scattered fields," *IEEE Transactions on Antennas and Propagation*, vol. 37, no. 7, pp. 918–926, 1989.

[26] GiD the personal pre and post processor, http://www.gidhome.com/home.

[27] W. C. Chew and Y. M. Wang, "Reconstruction of two-dimensional permittivity distribution using the distorted Born iterative method," *IEEE Transactions on Medical Imaging*, vol. 9, no. 2, pp. 218–225, 1990.

[28] L. Di Donato, R. Palmeri, G. Sorbello, T. Isernia, and L. Crocco, "Assessing the capabilities of a new linear inversion method for quantitative microwave imaging," *International Journal of Antennas and Propagation*. In press.

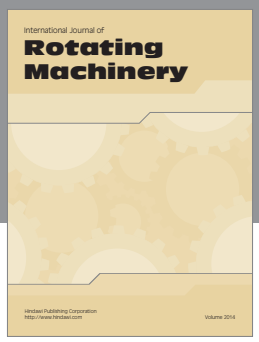

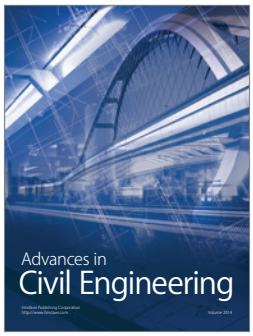

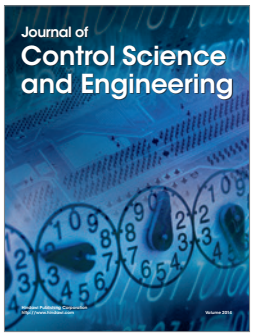

Hindawi

Submit your manuscripts at
http://www.hindawi.com